

The GMRT 325 & 610-MHz Cygnus survey: the Catalog

P. Benaglia^{1,2}, C. H. Ishwara-Chandra³, H. Intema^{4,5}, M. E. Colazo⁶, and M. Gaikwad⁷

¹ Instituto Argentino de Radioastronomía, CONICET & CICPBA, CC5 (1897) Villa Elisa, Prov. de Buenos Aires, Argentina
e-mail: paula@iar.unlp.edu.ar

² Facultad de Ciencias Astronómicas y Geofísicas, UNLP, Paseo del Bosque s/n, 1900, La Plata, Argentina

³ National Centre for Radio Astrophysics (NCRA-TIFR), Pune, 411 007, India

⁴ International Centre for Radio Astronomy Research, Curtin University, Bentley, WA 6102, Australia

⁵ Leiden Observatory, Leiden University, Niels Bohrweg 2, 2333 CA Leiden, the Netherlands

⁶ Comisión Nacional de Actividades Espaciales, Paseo Colón 751 (1063) CABA, Argentina

⁷ Max-Planck-Institut für Radioastronomie, Auf dem Hügel 69, D-53121 Bonn, Germany

Received xx, 2020; accepted YYY

ABSTRACT

Context. Observations at the radio continuum band below the GHz are key when investigating the nature and properties of non-thermal sources, since at those frequencies their radio radiation is strongest. Therefore, the low radio frequency range is the best to spot possible counterparts to very high-energy (VHE) sources: relativistic particles of the same population are prone to be involved in radio and high energy radiation processes. Some of those counterparts to VHE sources can be stellar sources.

Aims. The Cygnus region on the northern sky is one of the richest in this type of sources which are potential counterparts to VHE sources. We surveyed the central ~ 15 sq deg of the Cygnus constellation at the bands of 325 and 610 MHz, with angular resolutions and sensitivities of $10''$ and $6''$, and 0.5 and 0.2 mJy beam⁻¹, respectively.

Methods. The data were collected during 172 hours along 2013 – 2017, using the Giant Metrewave Radio Telescope (GMRT) with 32 MHz bandwidth, and were calibrated using the SPAM routines. The source extraction was carried out with the PyBDSF tool, followed by verification through visual inspection of every putative catalog candidate source, in order to determine its reliability.

Results. In this first paper we present the catalog of sources, consisting of 1048 sources at 325 MHz and 2796 sources at 610 MHz. By cross-matching the sources from both frequencies with the objects of the SIMBAD database, we found possible counterparts for 143 of them. Most of the sources from the 325-MHz catalog (993) were detected at the 610 MHz band, and their spectral index α was computed adopting $S(\nu) \propto \nu^\alpha$. The spectral indices distribution shows its maximum at $\alpha = -1$, characteristic of non-thermal emitters and possibly pointing at an extragalactic population.

Key words. Catalogs – Radio continuum: general – Open clusters and associations: individual: Cygnus OB2, OB8, OB9

1. Introduction

The first gamma-ray all-sky observations, obtained decades ago with the satellites COS-B (Hermesen et al. 1977, and references therein) and Compton (Hartman et al. 1999), disclosed numerous sources with no counterpart at other wavelengths, hereafter called unidentified gamma-ray sources or UNIDS. Since then, a large number of multi-frequency observations have been implemented to understand the nature of those sources (e.g. Paredes et al. 2008; Massaro et al. 2013). Despite significant improvement in the telescopes capabilities in sensitivity and resolution, there still remain thousands of gamma-ray sources to be identified. For instance, the fourth Fermi LAT catalog (The Fermi-LAT collaboration 2019, more than 5000 sources) listed about one third of the detected sources without any counterpart at lower energies. The sources detected with ground-based telescopes, at TeV energies, also present problems in conclusive identification; besides, their large position uncertainty precludes the correlation with individual objects (see for example the H.E.S.S. source catalog¹ and its identifications).

The identified gamma-ray sources are mostly AGNs, and pulsars, supernova remnants or high-mass X-ray binaries (HMXBs). These objects emit at radio wavelengths and are gen-

erally stronger at low radio frequencies (< 1 GHz) due to the nature of the spectra of synchrotron radiation. In this part of the electromagnetic spectrum, major catalogs and surveys lack angular resolution or sensitivity to seek for singular counterparts of UNIDS (e.g., the NRAO VLA Sky Survey, $\sim 45''$ and 1 mJy, or the Westerbork Northern Sky Survey, $\sim 54''$ and 3 mJy; Condon et al. 1998; Rengelink et al. 1997). Recently, other types of stellar sources have been proposed as possible gamma-ray emitters, and different scenarios were analyzed. Additionally to the well-studied microquasars (Romero et al. 2003), colliding wind binaries (Benaglia & Romero 2003), Herbig Haro and Young Stellar Objects (Bosch-Ramon et al. 2010; Araudo et al. 2007; Rodríguez-Kamenetzky et al. 2019), stellar bow shocks (Benaglia et al. 2010; del Valle & Pohl 2018; del Palacio et al. 2018), are capable of producing gamma-rays. A signature of high-energy emission is the presence of non-thermal radio emission, since particles from the same population are prone to be involved in processes at both energy ranges, radio via synchrotron process and VHE emission via the inverse-Compton scattering. On top of that, the determination of counterparts of gamma-ray sources through radio observations in star-forming regions will help to clarify the role of young stars and collective wind effects in the acceleration of galactic cosmic rays (e.g. Romero 2008).

¹ <https://www.mpi-hd.mpg.de/hfm/HESS/pages/home/sources/>

Garwood et al. (1988) at 1.4 GHz continuum, at $b = 0^\circ$, a resolution up to $4''$ and completely to about 30 mJy peak flux density. The results were complemented by those of Zoonematkermani et al. (1990) for $|b| < 0.8^\circ$ that provided angular resolution and flux limit alike. With the Texas Interferometer, Douglas et al. (1996) imaged the area at arcsec scale above flux densities of 0.25–0.4 Jy. Taylor et al. (1996) carried out Westerbork Synthesis Radio Telescope observations along the Galactic plane and for $|b| < 1.6^\circ$, at angular resolution of $\sim 1'$ detecting sources brighter than 10 mJy beam $^{-1}$.

In particular, Setia Gunawan et al. (2003) published the Westerbork Synthesis Radio Telescope 1400 and 325 MHz continuum survey of Cyg OB2, that attained angular resolutions of $13''$ and $55''$ and $5\text{-}\sigma$ flux density limits of ~ 2 mJy and $\sim 10\text{--}15$ mJy respectively. The authors detected, in an observed area of $2^\circ \times 2^\circ$, 210 discrete sources, 98 of them at both frequencies, plus 28 resolved sources.

The observations presented here were performed at two bands, centred at 325 and 610 MHz, with the GMRT, that allowed to map the continuum radio emission at arcsec resolution, and below the mJy sensitivity level. Some information about the observations was given in Ishwara-Chandra et al. (2019).

The observed region marked in Fig. 1 is displayed in equatorial coordinates in Fig. 2. The GMRT fields of view (FoV) HPBW are $81 \pm 4'$ at 325 MHz and $43 \pm 3'$ at 610 MHz³.

To cover the desired observing area we needed to point at five 325 MHz FoVs, and forty-seven 610 MHz FoVs. Some observations consisted of bad data so we repeated them with new observations (20 h). The pointings layout was chosen to yield a uniform noise while minimizing the number of them (i.e., the observing time). Figure 2 shows the disposition of the pointings and the FoVs at both observing bands. The project was divided in four observing campaigns, scheduled from November 2013 to September 2017. Table 1 lists the GMRT campaign ID, allocated time and year(s) of completion.

Details of the targeted areas and observing parameters are given in Table 2: the name of the FoV, the corresponding cam-

³ GMRT Observer's Manual; www.ncra.tifr.res.in/ncra/gmrt/gmrt-users/observing-help/manual_7jul15.pdf

We carried out a survey of the Cygnus Rift center with the GMRT, by means of continuum observations at two bands (325 MHz and 610 MHz), to investigate the non-thermal emission of the various types of sources present in this rich field and potential counterparts of UNIDS. With two frequencies, we were also able to get spectral information which could help to categorise certain classes and emission mechanisms on the basis of spectral index. Here we present the source catalog at each band, along with spectral index information when possible. In Section 2 we present the main characteristics of the Cygnus region and precedent studies at low frequency radio continuum; in Sect. 3 and 4 we describe how the observations were carried out, and the processes attached to data reduction to get the final images. Section 5 explains the data analysis performed on the images and how the sources were extracted. Section 6 contains the findings related to spectral indices for the sources detected at the two observing bands. In Section 7 we discuss the catalog main properties. Results on searching for counterparts are given in Sect. 8, and we close by mentioning related studies and prospects in the last Section.

2. The Cygnus region and radio observations background

The Cygnus Rift is a large area at northern declination, obscured by the dust of molecular clouds. It spans from $65^\circ \leq l \leq 95^\circ$ $-8^\circ \leq b \leq +8^\circ$, at a distance up to 2.5 kpc; see Reipurth & Schneider (2008) for a comprehensive review. As portrayed in Fig. 1 (Mahy et al. 2013), it encompasses nine OB associations and several bright open clusters, with signs of recent star formation. One of the youngest associations is Cyg OB2: it is also the richest one, with over hundred O stars and thousands of B stars, as reported by Knödlseder (2000). Next to OB2, Cyg OB8 and Cyg OB9 present hundreds of hot stars.

Since the project main goal was to relate non-thermal radio sources with stellar objects – stars at different evolutionary stages – we circumscribed the region under study to the the associations Cyg OB2, OB8 and OB9; its extension is displayed in Fig. 1 in Galactic coordinates, related to the Cygnus constellation. It covers ~ 15 sq deg. The associations Cyg OB8 and OB9 are not surveyed in full, since they are adjacent to strong and/or large sources (like the case of Cyg X–1 and Cyg A), which could introduce problems related to high-dynamic range imaging.

Below the Jy threshold, the Cygnus area was observed as part of Galactic plane surveys with the Very Large Array² by

² <https://science.nrao.edu/facilities/vla>

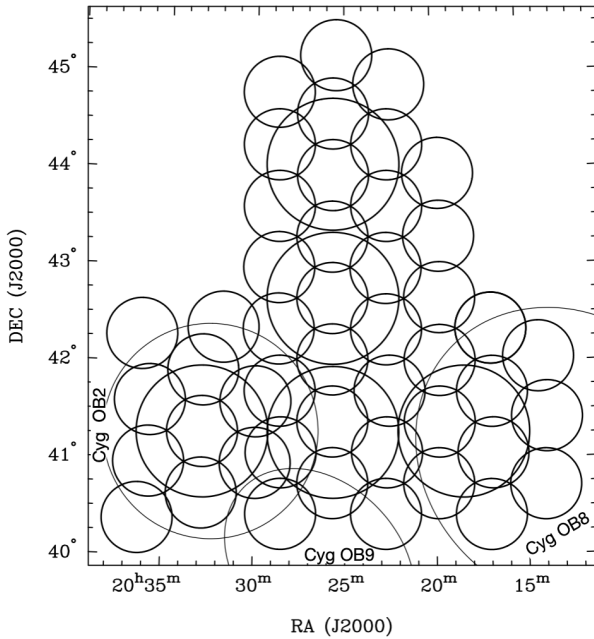


Fig. 2. Disposition of the pointings at 325 MHz (larger circles) and 610 MHz (smaller circles), showing the observed FoV half power beam widths. The extent of the stellar associations Cyg OB2, OB8 and OB9 (Uyaniker et al. 2001) is shown using thinner lines.

Table 1. Observing campaigns basic information.

#	Campaing ID	Time (h)	Obs. dates
1	25_026	12	2013
2	27_036	40	2014–2015
3	28_081	40	2015
4	30_027	60	2016–2017

paing ID, the exact date of observation, the position of the pointing center, the time on fields-of-view (t.o.s.), the band, and the calibrators used, ordered by band, and by right ascension. The observations were carried out using the total intensity mode and a bandwidth of 32 MHz and 256 spectral channels to minimise the effect of bandwidth smearing. Flux calibrators were observed at the start and end of the each run for flux and bandpass calibration. A phase calibrator was observed for 5 minutes after a scan of 30 minutes on the target to calibrate the phases and any slow variations of the gain of the telescope.

4. Data reduction

The five pointings at 325 MHz were processed uniformly, using the SPAM routines (Intema 2014), which is a python package based on the Astronomical Image Processing System (AIPS), for nearly automatic analysis of GMRT data below 1 GHz. Bad data and RFI were initially flagged at the full spectral resolution of 256 channels. The flux calibration was done using the primary calibrators 3C286, 3C48 and 3C147, and the scale by Scaife & Heald (2012) for low radio frequencies. The SPAM pipeline then converts the pre-calibrated visibility data to a final image, which includes several rounds of self-calibration and flagging iteratively, and wide-field imaging to correct for non-coplanarity. In the self-calibration, ionospheric phase corrections are computed for several directions within the field of view for direction dependent corrections on the integration timescales. The self-calibration procedure was followed using default parameters of

SPAM, with initial cycles in phase with long intervals and a last run with the solution interval of the visibilities integration time; in our case 16.9 seconds. Towards the end of the loop, one round of amplitude and phase self-calibration is carried out. During imaging, a moderately uniform weighting scheme (robust=−1 in AIPS) was used, however multi-scale cleaning options were not incorporated. Primary beam corrections were applied using the GMRT specific parameters (GMRT Observer’s Manual).

Since the target is in the galactic plane, the T_{sys} correction for excess background was applied using the 408 MHz all sky map (Haslam et al. 1982) during the calibration as part of the pipeline. The correction factor varied from 1.7 to 3.6, with the highest correction factor near the galactic plane and lower correction factor away from the plane. The FoVs were combined in a mosaic with weights as inverse of variance.

The data analysis of the forty-seven FoVs at 610 MHz were also carried using the SPAM pipeline similar to the 325 MHz data. The T_{sys} correction for the excess background at 610 MHz ranged from 1.22 to 1.76. The FoVs named FoV610.21 and FoV610.30 resulted noisier than the rest, probably due to the presence of strong extended emission from the galactic plane and bright sources in the fields.

The final mosaics presented average rms of $0.5 \text{ mJy beam}^{-1}$ and $0.2 \text{ mJy beam}^{-1}$ at 325 and 610 MHz, respectively, although, locally, values strongly depend mainly on the extended and/or diffuse emission. The synthesized beams attained were $10'' \times 10''$, and $6'' \times 6''$, and the mosaic image sizes resulted in (6487×6573) , and (12580×13837) pixels, respectively. The final images are presented in Figs. 3 & 4.

A note on the flux uncertainties here: there are a series of factors that impact in different ways on the accuracy of low-frequency radio flux scales. Along their observations with the GMRT, Chandra et al. (2004), for instance, discuss a flux scale uncertainty at 325 and 610 MHz of a few percent. Besides, in case of target fields in the galactic plane as the one presented here, the fact that T_{sys} can be significantly higher due to higher sky temperature than towards the calibrator imposes an additional correction factor; although the SPAM pipeline performs an estimation of this factor, it is based in some assumptions and extrapolations that may introduce some inaccuracy. We used different flux calibrators, the primary beam model is not perfect, and mosaicking different pointings into the final images used for source extraction can all affect the flux scale. Taking all the above into account, a very conservative approach will be to adopt flux density uncertainties of 10%.

5. Source extraction

When the mosaics at the two observing bands were built, we checked for errors in astrometry. First, by taking into consideration point sources along the entire two images. We did not find significant errors at the smaller pixel scale, i.e., accuracy was better than 1.5 arcseconds. And secondly, among the 610 MHz image and point sources with optical positions well determined: Wolf-Rayet and O-type stars. For the cases with radio emission at or near the position of those stars (13 in total), the differences in coordinates were in the range $0.1 - 3.1''$, with a standard deviation of $1.34''$ (see Benaglia et al. 2020, for a study of the massive, early-type stars detected using the current databases).

To survey the emission present at the 325 and 610 MHz images, we applied the Python Blob Detector and Source Finder (PyBDSF⁴). The tool can be used to find islands of emission

⁴ <http://www.astron.nl/citt/pybdsf/>

Table 2. Observing runs and fields of view information.

Field of view name	Campaign ID	Observing dates	Pointing center (J2000)		t.o.s. (min)	Band (MHz)	Calibrators
			RA (h,m,s)	Dec (deg,′,″)			
FoV325.1	27_036	7/2,26/9/15	20 18 26	41 16 50	488	325	3C48,2052+365
FoV325.2	27_036	26/10/14	20 25 38	41 16 50	304	325	3C48,2052+365
FoV325.3	27_036	27/10/14	20 25 38	42 39 50	296	325	3C147,2052+365
FoV325.4	27_036	6/2/15	20 25 38	44 02 50	283	325	3C48,2052+365
FoV325.5	25_026	4/11/13	20 32 50	41 16 50	523	325	3C48,2038+513
FoV610.1	28_081	18/6/15	20 13 50	41 21 15	79	610	3C48,2052+365
FoV610.2	28_081	18/6/15	20 13 60	40 43 10	79	610	3C48,2052+365
FoV610.3	30_027	11,21/8/16	20 14 13	42 02 30	118	610	3C48,3C286,2052+365
FoV610.4	28_081	18/6/15	20 16 50	41 03 15	130	610	3C48,2052+365
FoV610.5	28_081	25/7/15	20 16 50	41 41 20	119	610	3C48,2052+365
FoV610.6	30_027	2/9/17	20 16 50	42 20 30	69	610	3C48,2052+365
FoV610.7	28_081	25/7/15	20 17 00	40 25 05	71	610	3C48,2052+365
FoV610.8	30_027	17/7,8/8/16	20 19 40	42 40 01	147	610	3C48,2052+365
FoV610.9	30_027	17/7,8/8/16	20 19 40	43 18 01	179	610	3C48,2052+365
FoV610.10	30_027	17/7/16	20 19 40	43 56 56	78	610	3C48,2052+365
FoV610.11	30_027	1/7/16	20 19 42	42 01 08	94	610	3C286,2052+365
FoV610.12	28_081	25/7/15	20 19 45	41 22 60	119	610	3C48,2052+365
FoV610.13	28_081	15/8/15	20 19 50	40 44 50	119	610	3C48,2052+365
FoV610.14	30_027	15/7/16	20 22 25	44 52 09	64	610	3C48,2052+365
FoV610.15	28_081	16/8/15	20 22 30	41 42 30	119	610	3C48,2052+365
FoV610.16	30_027	2/9/17	20 22 34	44 15 01	59	610	3C48,2052+365
FoV610.17	30_027	2/9/17	20 22 36	43 36 53	59	610	3C48,2052+365
FoV610.18	28_081	15/8/15	20 22 40	41 04 20	107	610	3C48,2052+365
FoV610.19	30_027	30/6,23/7/16	20 22 40	42 20 30	168	610	3C48,3C286,2052+365
FoV610.20	30_027	30/6,23/7/16	20 22 40	42 58 30	231	610	3C48,3C286,2052+365
FoV610.21	28_081	15/8/15	20 22 45	40 26 15	62	610	3C48,2052+365
FoV610.22	30_027	15/7/16	20 25 27	45 10 21	71	610	3C48,2052+365
FoV610.23	30_027	2/9/17	20 25 38	43 56 06	76	610	3C48,2052+365
FoV610.24	30_027	2/9/17	20 25 38	44 34 14	70	610	3C48,2052+365
FoV610.25	28_081	16/8/15	20 25 40	40 45 25	119	610	3C48,2052+365
FoV610.26	28_081	17/8/15	20 25 40	41 23 35	142	610	3C48,2052+365
FoV610.27	30_027	14/7/16	20 25 40	42 01 60	89	610	3C48,2052+365
FoV610.28	30_027	30/6,23/7/16	20 25 40	42 40 00	168	610	3C48,3C286,2052+365
FoV610.29	30_027	1,2,24/7/16	20 25 40	43 18 00	243	610	3C48,3C286,2052+365
FoV610.30	28_081	17/8/15	20 28 30	40 26 15	79	610	3C48,2052+365
FoV610.31	28_081	16/8/15	20 28 30	41 04 20	71	610	3C48,2052+365
FoV610.32	28_081	17/8/15	20 28 35	41 42 30	79	610	3C48,2052+365
FoV610.33	30_027	1,2,24/7/16	20 28 40	42 21 00	232	610	3C48,3C286,2052+365
FoV610.34	30_027	1,2,24/7/16	20 28 40	42 59 00	230	610	3C48,3C286,2052+365
FoV610.35	30_027	1/7/16	20 28 40	43 36 53	94	610	3C286, 2052+365
FoV610.36	30_027	1/7/16	20 28 42	44 15 01	94	610	3C286, 2052+365
FoV610.37	30_027	15/7/16	20 28 44	44 47 32	71	610	3C48, 2052+365
FoV610.38	27_036	28,29/11/14	20 29 55	40 57 38	120	610	3C48,2052+365
FoV610.39	27_036	28,29/11/14	20 29 55	41 35 45	120	610	3C48,2052+365
FoV610.40	30_027	17/7,8/8/16	20 31 45	42 21 39	145	610	3C48,2052+365
FoV610.41	27_036	28,29/11/14	20 32 50	40 38 42	120	610	3C48,2052+365
FoV610.42	30_027	14/7,8/8/16	20 32 50	41 16 50	165	610	3C48,2052+365
FoV610.43	27_036	28,29/11/14	20 32 50	41 54 58	120	610	3C48,2052+365
FoV610.44	27_036	28,29/11/14	20 35 45	40 57 38	105	610	3C48,2052+365
FoV610.45	27_036	28,29/11/14	20 35 45	41 35 45	120	610	3C48,2052+365
FoV610.46	30_027	8,11,21/8/16	20 36 17	40 22 30	177	610	3C48,3C286,2052+365
FoV610.47	30_027	11,21/8/16	20 36 17	42 16 30	118	610	3C48,3C286,2052+365

in radio interferometry images, decompose them into Gaussian functions, and finally gather them into individual source fits. We chose a signal-to-noise of 7 as the lower limit for a source/fit to be accepted, proceeding in the same way as in Benaglia et al. (2019) where proved successful. A similar detection threshold was used for the CORNISH catalog (Purcell et al. 2013). The

routine includes the determination of the rms along the image, and the production of a corresponding rms image.

The running of PyBDSF over the 325 and 610 MHz image mosaics resulted in 1230 and 3023 sources respectively. After a thorough visual inspection, of each source, we kept 1048

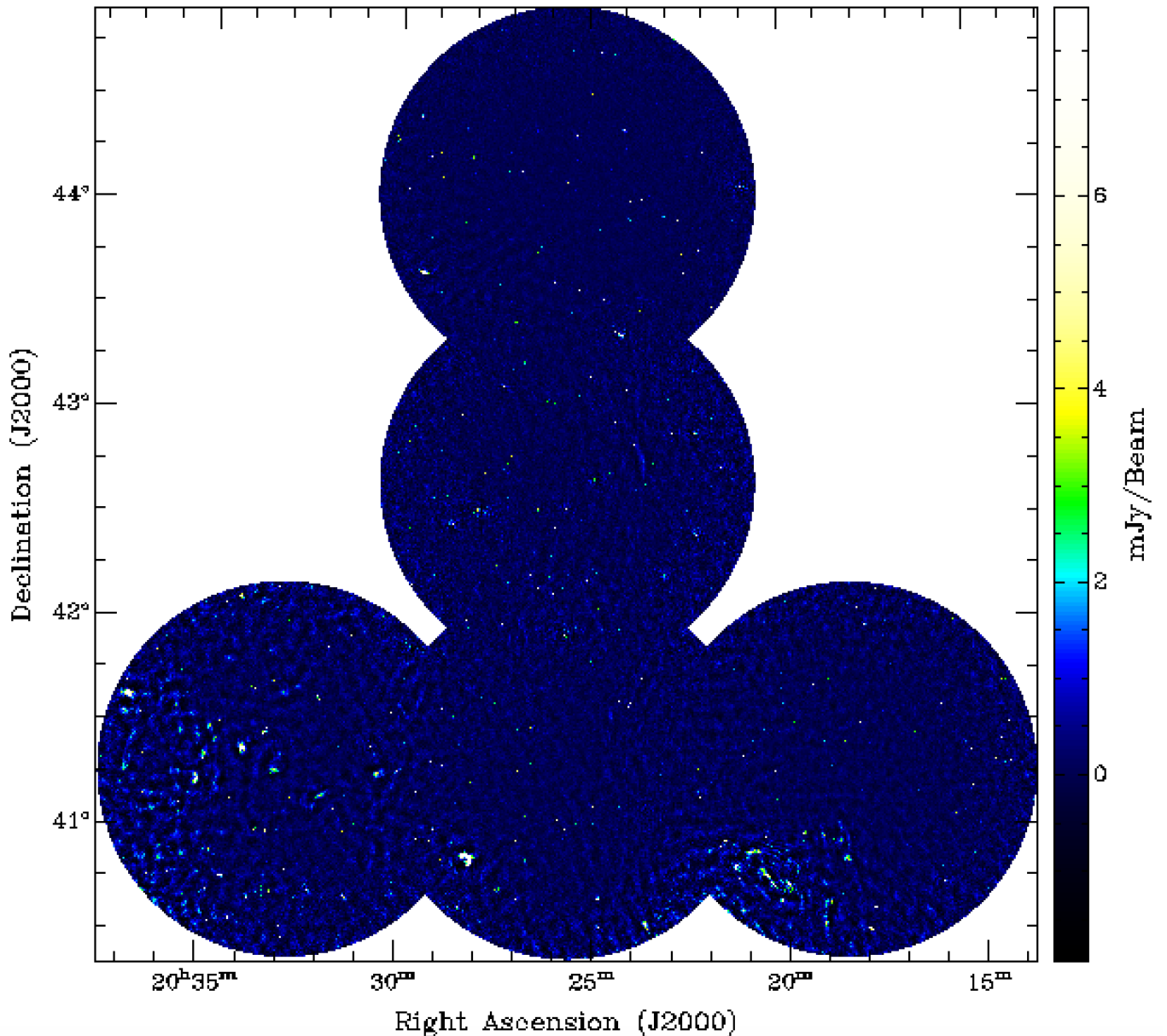


Fig. 3. GMRT 325-MHz continuum image of the observed field. The synthesized beam is $10'' \times 10''$ and the average rms is $0.5 \text{ mJy beam}^{-1}$. The full range flux density values are $-9.2, +812.5 \text{ mJy beam}^{-1}$. The interval shown is $(-2, +8) \text{ mJy beam}^{-1}$, to outline the weaker features.

(85.2%) from the 325 MHz image, and 2796 (92.5%) from the 610 MHz image.

The group of the accepted entries consisted of discrete (unresolved) objects represented by one fitted source of the size of the synthesized beam, and of resolved objects. Some resolved objects were represented by a fitted source, larger in size than the synthesized beam, while others were described by a combination of fitted sources.

We rejected fits to filaments and (part of) diffuse emission (3.5% at 325 MHz and 1.5% at 610 MHz, see Fig. 5-a) and those fit combinations corresponding to strong and/or large objects with ill-representations (1.7% at 325 MHz and 2.0% at 610 MHz; Fig. 5-b). We also discarded either objects with reduction artifacts that preclude a proper fit (including end-of-field objects: 2.5% at 325 MHz and 8.2% at 610 MHz, Fig. 5-c) and fitted sources similar to surrounding noise (1.5% at 325 MHz and 1.3% at 610 MHz, see Fig. 5-d).

Overall, the 610 MHz emission could be better imaged by the SPAM pipelines than that at the lower frequency band. The 325 MHz mosaic presented a larger percentage of extended emission fitting problems. The largest detectable structure is $32'$ at the 325 MHz band, and $17'$ at the 610 MHz band (GMRT User's Manual): the data presented here is biased against structures larger than that. The selection of the robust weighting of -1 , a compromise between high angular resolution and signal-to-noise, outlined discrete sources over diffuse emission.

The attained rms at the two bands, besides intrinsic values contributed by the stellar sources under observation, are indeed a function of the time-on-source (here, time-on-fields). To check for the completeness of the sources detected above 7σ (7 rms), we also ran the PyBDSF routines using a detection threshold of 5σ . The fitted sources resulted 1721 at 325 MHz and 5015 at 610 MHz, well above the numbers found for the first run. When we visually inspected, several faint sources appeared like noise peaks which prompted us to use 7σ where significantly much

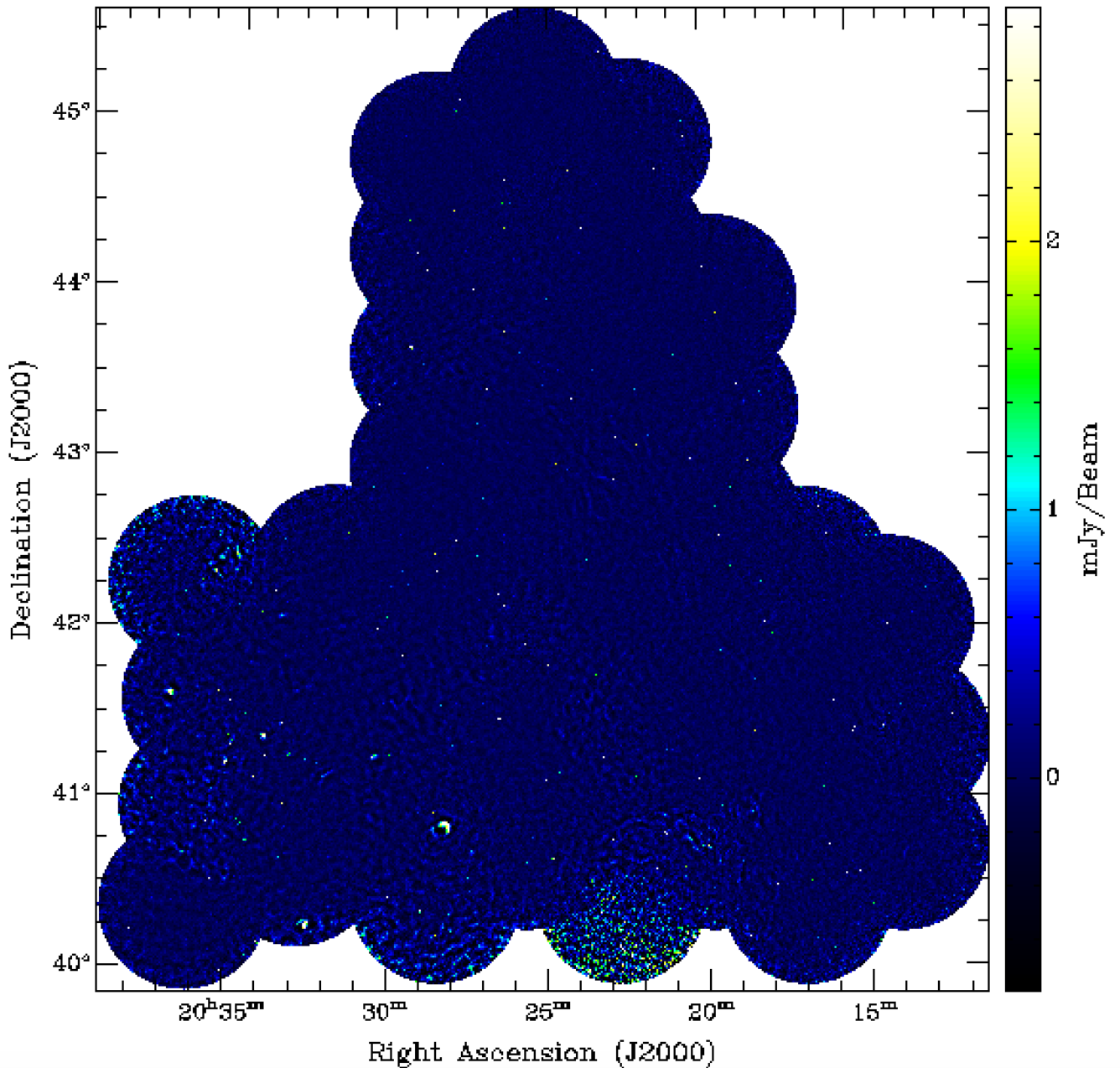


Fig. 4. GMRT 610-MHz continuum image of the observed field. The synthesized beam is $6'' \times 6''$ and the average rms is $0.2 \text{ mJy beam}^{-1}$. The full range flux density values are $-6.3, +928.3 \text{ mJy beam}^{-1}$. The interval shown is $(-0.8, +2.9) \text{ mJy beam}^{-1}$, to outline the weaker features.

less number of spurious sources were found. The incompleteness of the present catalog has been mainly quantified by the reasons given above regarding the fits.

The final lists of the accepted objects are reunited in the present Catalog. The cataloged sources are given in Tables 3 and 4, named consecutively (column 1) by increasing right ascension; only sample records are shown. We have tagged the sources with the label “BIC” followed by the observing frequency in MHz, and then a correlative number, based on their order. For each source, we list the coordinates RA, Dec (J2000) of the fit (columns 2 and 3), the integrated flux (column 4), the peak flux (column 5) and the fitted major axis, minor axis, and position angle (θ_1, θ_2 and PA , columns 6 to 8), that represent the source size and orientation after deconvolution, all with their corresponding errors as reported by PyBDSF. Full tables 3 and 4 will be provided as on-line material.

6. Spectral indices determination

The spectral index α of a source is a key parameter when investigating the source nature. If the flux densities at frequency bands centred at ν_1 and ν_2 are S_1 and S_2 , and $S_\nu \propto \nu^\alpha$, $\alpha = \log(S_1/S_2)/\log(\nu_1/\nu_2)$. In the case of the observations processed in this work, $\nu_1 = 325 \text{ MHz}$ and $\nu_2 = 610 \text{ MHz}$, and α can be derived if a source was detected at both bands.

In the process of obtaining spectral index information, we checked whether the sources detected at one of the observing bands were positionally coincident with one or more sources detected at the other band. To do that, we determined for each 325-MHz source ellipse if there was an overlap with any or more of the 610-MHz source ellipses. If true, we classified the overlapping as *partial*, when the ellipse at 325-MHz partially overlapped that at 610 MHz, or *full*, when the 610-MHz ellipse was

Table 3. Detected sources at 325 MHz above the 7σ level (first records); full table, 1048 records, as online material.

ID	RA_{J2000} (h,m,s)	Dec_{J2000} (deg,′,″)	Total flux (mJy)	Peak flux (mJy)	θ_1 (″)	θ_2 (″)	PA (°)
BIC325-0001	20:13:54.55±0.049	41:32:32.01±0.88	4.7±1.00	2.8±0.40	13.9±2.10	13.9±2.10	16.0±46.54
BIC325-0002	20:13:56.45±0.025	41:33:06.07±0.30	16.7±1.19	7.7±0.39	17.2±0.97	17.2±0.97	56.4±6.23
BIC325-0003	20:14:04.78±0.024	40:56:14.47±0.27	5.1±0.63	5.0±0.36	10.8±0.83	10.8±0.83	93.3±21.93
BIC325-0004	20:14:07.82±0.037	41:02:47.35±0.61	3.4±0.69	2.8±0.36	11.2±1.44	11.2±1.44	7.9±87.95
BIC325-0005	20:14:17.56±0.003	41:29:24.16±0.03	80.9±0.83	58.9±0.38	12.9±0.09	12.9±0.09	77.2±179.64
BIC325-0006	20:14:18.62±0.007	41:18:10.88±0.07	43.3±0.97	25.0±0.38	14.5±0.24	14.5±0.24	74.8±1.70
BIC325-0007	20:14:19.17±0.003	41:29:36.95±0.04	54.7±0.79	42.2±0.38	12.0±0.11	12.0±0.11	73.0±1.59
BIC325-0008	20:14:24.35±0.012	41:41:32.07±0.36	24.3±1.48	10.4±0.38	18.5±0.91	18.5±0.91	110.5±3.29
BIC325-0009	20:14:27.13±0.036	41:17:52.59±0.36	6.5±0.85	4.4±0.37	13.7±1.28	13.7±1.28	76.4±14.16
BIC325-0010	20:14:29.42±0.014	41:41:32.46±0.13	24.1±1.04	14.0±0.41	15.4±0.51	15.4±0.51	81.4±2.61

Notes. θ_1 , θ_2 , and PA represent the elliptic source size and orientation, and correspond to the the major axis, the minor axes and the position angle of the fit by the PyBDSM routines.

Table 4. Detected sources at 610 MHz above the 7σ level (first records); full table, 2796 records, as online material.

ID	RA_{J2000} (h,m,s)	Dec_{J2000} (deg,′,″)	Total flux (mJy)	Peak flux (mJy)	θ_1 (″)	θ_2 (″)	PA (°)
BIC610-0001	20:11:32.02±0.009	40:53:10.84±0.10	14.5±0.69	7.8±0.26	9.3±0.34	9.3±0.34	63.3±3.83
BIC610-0002	20:11:33.03±0.001	40:53:18.92±0.02	63.8±0.75	42.0±0.24	7.9±0.06	7.9±0.06	60.6±1.35
BIC610-0003	20:11:34.94±0.009	41:31:49.27±0.09	12.5±0.63	7.9±0.26	8.8±0.33	8.8±0.33	112.7±2.90
BIC610-0004	20:11:48.15±0.019	40:51:32.52±0.25	2.3±0.40	2.3±0.23	6.6±0.73	6.6±0.73	53.2±23.77
BIC610-0005	20:11:53.58±0.007	40:48:39.49±0.11	8.6±0.50	6.4±0.24	7.4±0.29	7.4±0.29	128.0±11.67
BIC610-0006	20:11:55.45±0.008	42:13:40.96±0.11	4.3±0.33	4.1±0.19	6.3±0.30	6.3±0.30	106.9±27.75
BIC610-0007	20:11:56.63±0.014	42:13:37.89±0.24	2.4±0.34	2.2±0.19	6.7±0.60	6.7±0.60	142.6±23.84
BIC610-0008	20:11:58.89±0.009	41:47:49.24±0.18	2.0±0.27	2.6±0.18	5.6±0.42	5.6±0.42	1.1±21.54
BIC610-0009	20:11:59.38±0.007	40:28:25.33±0.09	7.6±0.44	6.7±0.23	6.8±0.25	6.8±0.25	57.4±11.20
BIC610-0010	20:12:00.79±0.018	42:02:34.40±0.28	2.1±0.34	1.8±0.17	6.7±0.69	6.7±0.69	134.7±70.97

Notes. θ_1 , θ_2 , and PA represent the elliptic source size and orientation, and correspond to the the major axis, the minor axes and the position angle of the fit by the PyBDSM routines.

contained into the 325-MHz one. For *partial* cases, we registered the percentage of overlapping area (OA).

We then studied the 610-MHz ellipse/s that was/were related to each single 325-MHz one, and calculated a corresponding 610-MHz contributing flux SC_2 to use in the spectral index expression, in the following way. For *full* cases, we considered $SC_2 = S_2$. For *partial* cases, we set $SC_2 = S_2$ if $OA \geq 70\%$, $SC_2 = 0.5 S_2$ if $70\% > OA > 30\%$, and $SC_2 = 0$ elsewhere. We found that 993 sources at 325-MHz have one or more 610-MHz sources overlapped, and computed the corresponding spectral indices, considering for each source at 325 MHz all the overlapping sources at 610 MHz with the weights as explained above. Table 5 lists the 325 MHz source with its central coordinates, the 610 MHz source(s) that are partially or fully overlapping the former, and the spectral index α as derived from S_1 and SC_2 (a few records; full table as online material). We present the spectral index uncertainty by error propagation in the very conservative case, that is, using the flux density errors given by PyBDSF combined with a 10% error for flux density scales (see Sect. 4).

To evaluate the probability of random matches when deriving spectral indices, we calculated the inverse of the number of sources per sq deg over the area of the synthesized beam. At 325 MHz, we obtained that there will be one such a coincidence above 1700 sources. At 610 MHz, the probability of a random match is of one source of 3230. We found 1048 sources at 325 MHz, and 2796 sources at 610 MHz, thus assume that

is very unlikely that overlapping for unrelated sources has taken place.

7. Catalog properties

7.1. Detections, flux densities and noise levels

The Catalog comprises 1048 sources at 325 MHz and 2796 sources at 610 MHz with flux densities greater than 7σ ; here σ represents the local rms noise at the source surroundings. The sources are characterised by their integrated and peak flux densities with corresponding errors, major and minor axes and position angle of a fitted ellipse also with their errors.

Fig. 6 displays the distribution of the flux density of the sources detected at the 325 MHz band. In the lower panel we present a zoom on the flux interval 0 – 30 mJy, that contains 80% of the sources. And the corresponding histograms for 610 MHz appear in Fig. 7, with 91% of the sources with fluxes up to 30 mJy. At both bands the effect of favouring higher resolution (meanwhile outlining more-discrete sources) by means of the weighting scheme is appreciable as a majority of lower-fluxes sources. The detail in lower-flux sources show the typical decrease with flux (see for instance Fig. 3 in Zoonematkermani et al. 1990). The lower number of sources up to 5 mJy at 325 MHz is probably the effect of the detection threshold at that band (≈ 2 mJy on average).

Table 5. Sources detected at both frequency bands (325 and 610 MHz) and spectral index information (first records); full table, 993 records, as online material.

ID at 325MHz	RA, Dec _{J2000} (hms, dms)	ID at 610MHz	$\alpha_{610\text{MHz}}^{325\text{MHz}}$
BIC325-0002	20:13:56.45, 41:33:06.07	BIC610-0104,-0105	-0.4±0.26
BIC325-0003	20:14:04.78, 40:56:14.47	BIC610-0109	-0.7±0.32
BIC325-0004	20:14:07.82, 41:02:47.35	BIC610-0112	-1.4±0.48
BIC325-0005	20:14:17.56, 41:29:24.16	BIC610-0123	-1.1±0.23
BIC325-0006	20:14:18.62, 41:18:10.88	BIC610-0124	-1.0±0.23
BIC325-0007	20:14:19.17, 41:29:36.95	BIC610-0126	-0.9±0.23
BIC325-0008	20:14:24.35, 41:41:32.07	BIC610-0133,-0134,-0131	-0.8±0.25
BIC325-0009	20:14:27.13, 41:17:52.59	BIC610-0140	-1.2±0.34
BIC325-0010	20:14:29.42, 41:41:32.46	BIC610-0146	-1.3±0.24
BIC325-0012	20:14:30.76, 41:41:41.64	BIC610-0147	-0.9±0.25

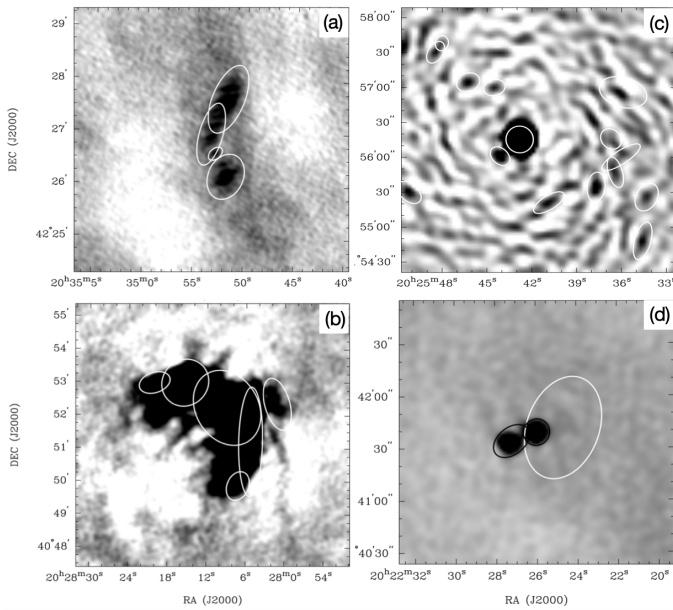


Fig. 5. Examples of discarded fits, for the four cases given in Sect. 5, represented as white-line ellipses. (a): Filaments and/or diffuse emission at 610 MHz. (b): Strong/large sources ill represented by a combination of fits at 325 MHz. (c): Reduction artifacts at 325 MHz. (d): Fits of emission similar to the noise at 610 MHz; in this last case, the fits accepted as good ones are shown with black-line ellipses.

We compared the number of sources here detected with the results from other studies. At the 325 MHz band, the survey by Taylor et al. (1996), carried out with the WSRT at 327 MHz, reported 3984 sources, over a detection threshold of 10 mJy, a 160-sq deg area, and angular resolution $\geq 1'$, which means a ratio R of 24.9 sources per square degree. At a similar frequency, we obtained 453 sources with fluxes above 10 mJy, thus a ratio of 40.1 sources per sq deg. The difference can be explained in terms of the larger beam used by the former survey, six times the synthesised beam used here, since some nearby GMRT sources will be seen as one WSRT source. A quick comparison with Setia Gunawan et al. (2003)'s detections (synthesised beam > 5 times that of this research) resulted in the recovery of more than 90% of their sources present in the area in common.

The VLA FIRST survey (Becker et al. 1995), performed at 20 cm, found 946432 sources above a detection threshold of 1 mJy (0.15 mJy rms), using angular resolution images of $\sim 5''$, over an area of 10575 sq deg, and then $R = 89.5$. The FIRST detection limit will correspond to a value of 1.8 mJy, if scaled to the

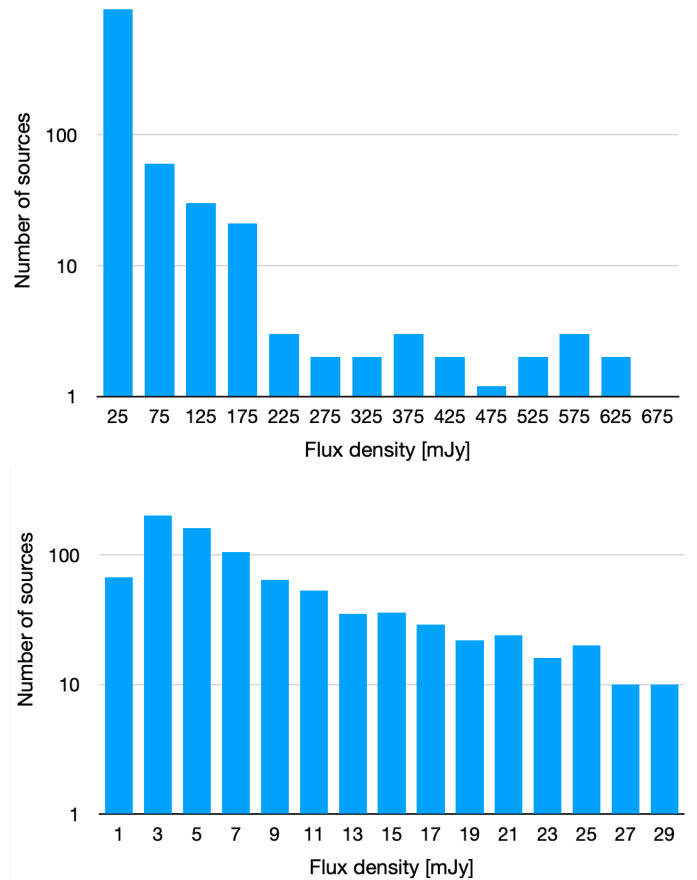


Fig. 6. Top: Number of sources as a function of their integrated flux density, for 99.71% of the sources cataloged at 325 MHz. Bottom: idem for flux densities up to 30 mJy (841 –80%– sources out of 1048).

610 MHz band using a spectral index of -0.7 . In the present catalog, near 1800 sources showed flux densities larger than 1.8 mJy, and $R = 91.4$, in very good agreement with the results from Becker et al. (1995).

Regarding the rms per pixel at each band, we present in Fig. 8 the histograms showing the distribution of the rms along the fields observed, as obtained when applied the PyBDSF routines, at both bands. This rms value is estimated by PyBDSF near each source before fitting. At 325 MHz, 88% of the pixels show rms up to 0.5 mJy beam $^{-1}$. At 610 MHz, 80% of the pixels show rms up to 0.2 mJy beam $^{-1}$. We also performed a comparison between those rms values and the rms values of a residual image where

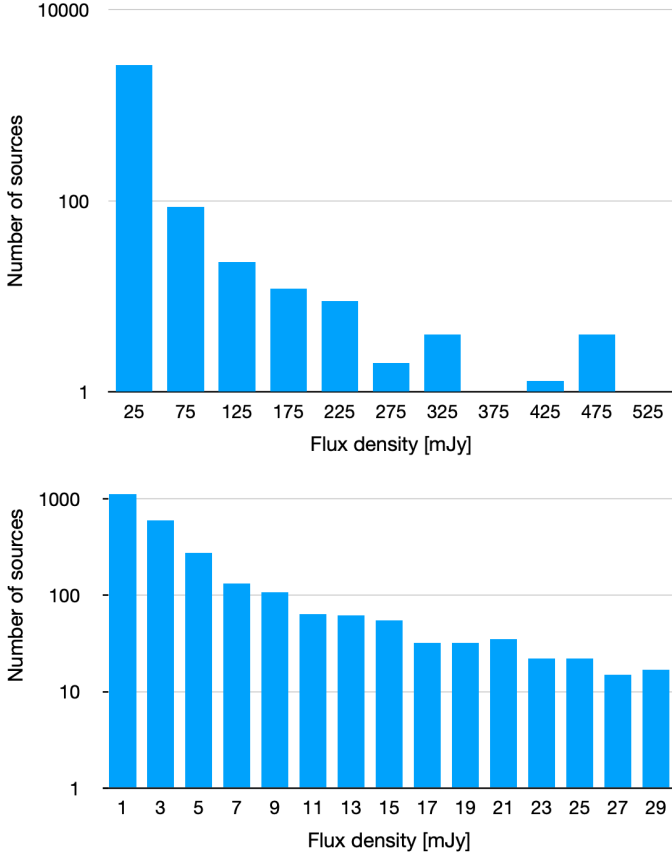


Fig. 7. Top: Number of sources as a function of their integrated flux density, for 99.75% of the sources cataloged at 610 MHz. Bottom: idem for flux densities up to 30 mJy (2565 –91%– sources out of 2796).

the contribution of the fitted sources had been subtracted. The results are presented in Fig. 9. It can be appreciated that the rms values decrease considerably, as expected.

7.2. Resolved and unresolved sources

To discriminate between resolved and unresolved sources, we plotted in Figure 10 the ratio of the total (integrated) flux over the peak flux for circular sources ($\theta_1/\theta_2 < 1.05$, 418 sources) at 610 MHz. The ratio remains below 1.25 out to $6.6''$, that we adopt as the dividing line between resolved and unresolved sources. This value happens to be the size of the synthesised beam plus a 10% error, at that frequency. We apply the same criterion based on the ratio value of 1.25 for the sources detected at 325 MHz. The distribution of the mean axes (sizes) of the cataloged sources, in the form of the average of the major and minor axes of each ellipse, is shown in Figs. 11 and 12.

7.3. Source multiplicity

During the visual inspection process of all sources found at both bands, we marked those characterized by adjacent emission components, fit by distinct Gaussian functions. In many of them, even a bridge linking components was clearly seen. Following the technique by Magliocchetti et al. (1998) and Huynh et al. (2005), we listed the sources that presented a companion up to $2'$, and discriminated the pairs (source+companion) where the flux density ratio (brighter over weaker) remained below 4. Fig. 13 shows the representation of these groups in the plane of

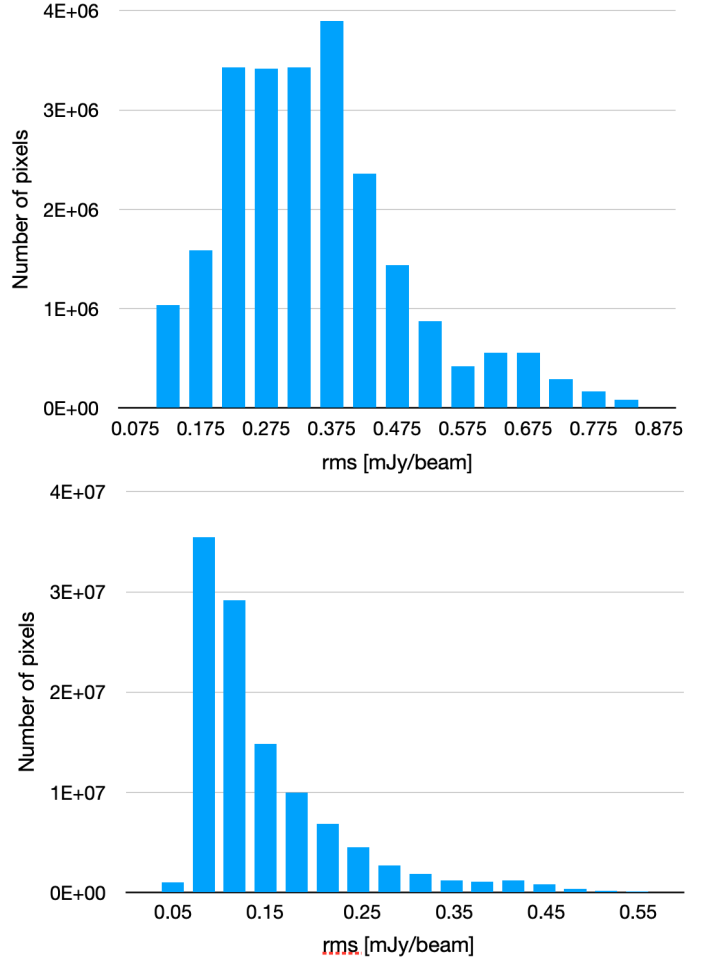


Fig. 8. Distribution of rms along the mosaics at 325 MHz (top panel) and at 610 MHz (bottom panel).

the sum of the fluxes (FS) of the components for each pair versus the separation (x) between components.

Two areas are appreciated in the plots at both bands, depending whether they contain visually-checked double pairs. The mentioned previous works found that the limit between areas could be described by $FS \propto x^2$. The data presented here seems to be better confined with an exponential of 3.5; see Fig. 13, where we have plotted both limiting lines. In principle, one can infer that for those pairs lying in the left areas their components are more probable to be physically related.

7.4. Spectral indices considerations

In the case of the spectral index distribution of the ~one thousand sources detected at two bands in the present Catalog, the pronounced maximum at $\alpha = -1$ confirms the non-thermal nature of the majority of the sources, see Figs. 14 and 15. The median error in α is 0.29. The spectral index values span from -3.06 to $+1.41$. Only four out of 993 values are below -2.5 . Variability can be one of the reasons for the index extreme absolute values: the two frequency data were taken at different times. Also, they might be consequence of applying the systematic pondering of the fluxes for sources not fully overlapping.

The uncertainties on the spectral indices are somewhat large which is due to conservative error on flux density as well as due to the two frequencies are only about a factor of two apart. How-

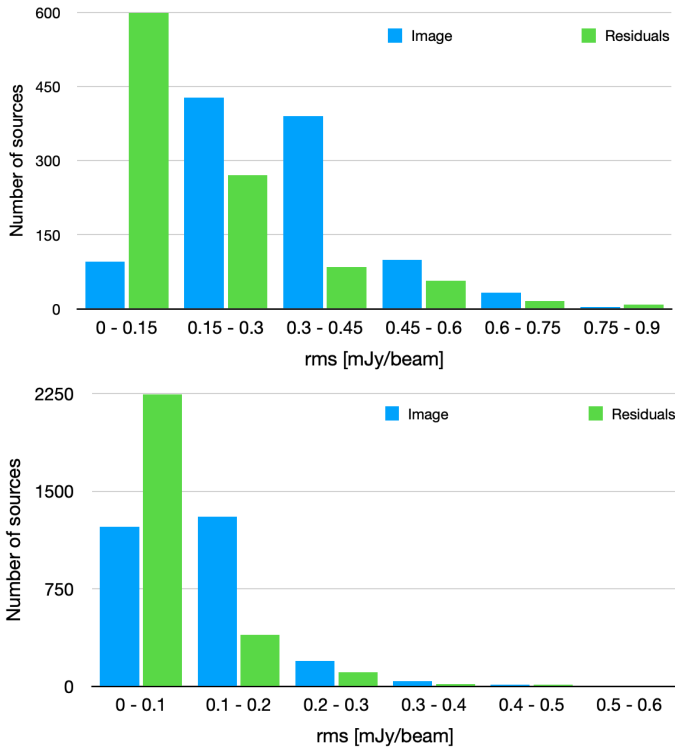


Fig. 9. Distribution of rms along the mosaics before (light blue bars) and after source extraction (green bars) at 325 MHz (top panel) and at 610 MHz (bottom panel).

ever, this should be sufficient to broadly categorise the sources as thermal, non-thermal or to pick up sources with very steep spectra.

Those 993 sources with spectral index value, detected at the 325 MHz band, correspond to 1065 sources at the 610 MHz band: at this latter frequency, the synthesized beam is smaller, and we found two or even three 610 MHz sources that overlap to the same 325 MHz object; see Table 5. The surveyed area at 325 MHz totaled 23486672 pixels with signal (pixel size = $2.5'' \times 2.5''$), or 11.3 sq deg. At 610 MHz, 113370869 pixels with signal accounted for 19.7 sq deg (pixel size = $1.5'' \times 1.5''$). At the same area covered by the 325-MHz mosaic, 1796 sources at 610 MHz (out of the total number of 2796) were fitted, thus the ratio of source-fits at 610 to 325 MHz is 1.71. This can be explained by sensitivity limitations, considering that at 610 MHz we have better angular resolution and lower noise, allowing to detect thermal sources that will remain undetected at 325 MHz, because also they are fainter, apart from the cases when we are picking at 610-MHz more than one source counterpart of a single 325 MHz source.

8. Search for counterparts

Once the catalog of 325 and 610 MHz sources was completed, we searched for nearby objects as possible counterparts to the (1048+2796=) 3844 entries. We used the Simbad database⁵, with two input tables: one containing the coordinates of the records of the 325 MHz sources, and a second one with those of the 610 MHz sources. The search radius was set as the semi-major axis of the ellipse fit of each record. We found possible counterparts for 85 sources at 325 MHz and for 138 sources at

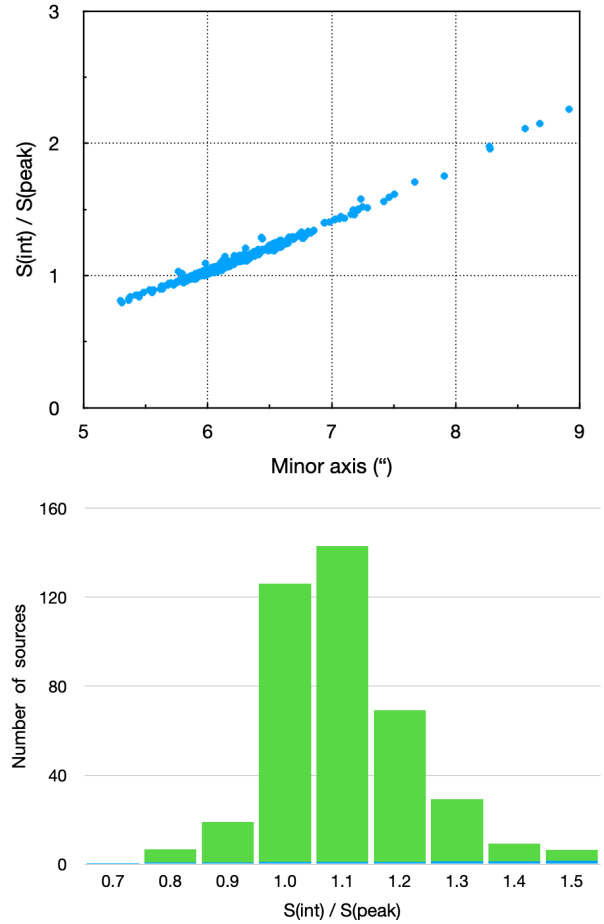


Fig. 10. Top panel: Ratio of total flux over peak flux as a function of their minor axis, for sources with $\theta_1/\theta_2 \leq 1.05$, catalogued at 610 MHz. A power fit yields $S_{\text{int}}/S_{\text{peak}} = 1.25$ at $\theta_2 = 6.6''$. Bottom panel: distribution of the flux ratio of the same group of sources.

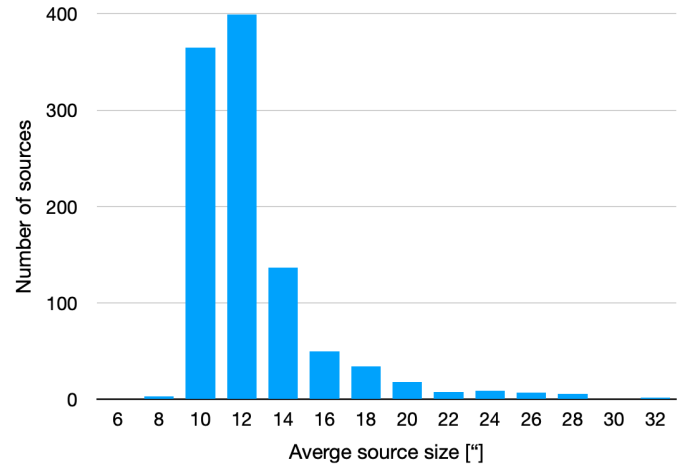


Fig. 11. Distribution of average axis $[0.5 \times (\text{major axis} + \text{minor axis})]$ of the ellipses representing the sources at 325 MHz.

610-MHz, where for some sources, more than one nearby object was found. We studied in each case all possible counterparts, checking also that the nearby object were inside the fitted ellipse -thus, taking into consideration the semi-minor axis and position angle of the source fit. We gathered the findings in Table 6, that presents possible counterparts for 5 sources only detected

⁵ <http://simbad.u-strasbg.fr/simbad/sim-fid>

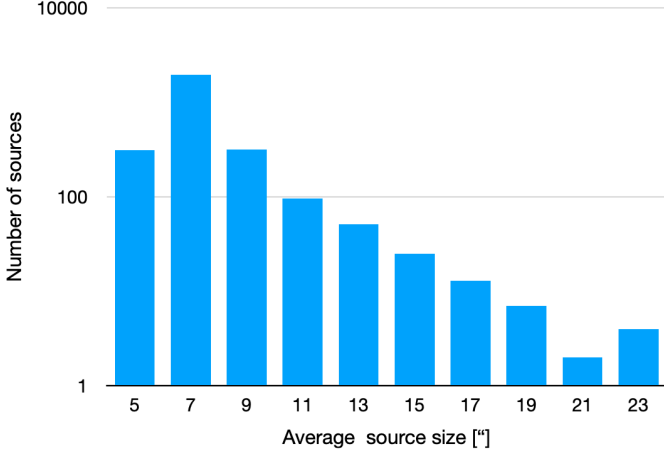


Fig. 12. Distribution of average axis [$0.5 \times (\text{major axis} + \text{minor axis})$] of the ellipses representing the sources at 610 MHz.

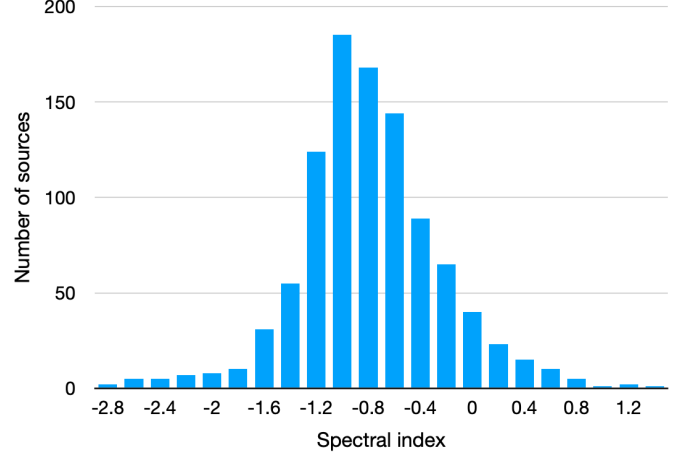


Fig. 14. Distribution of spectral indices corresponding to the sources detected at both frequency bands (see Table 5).

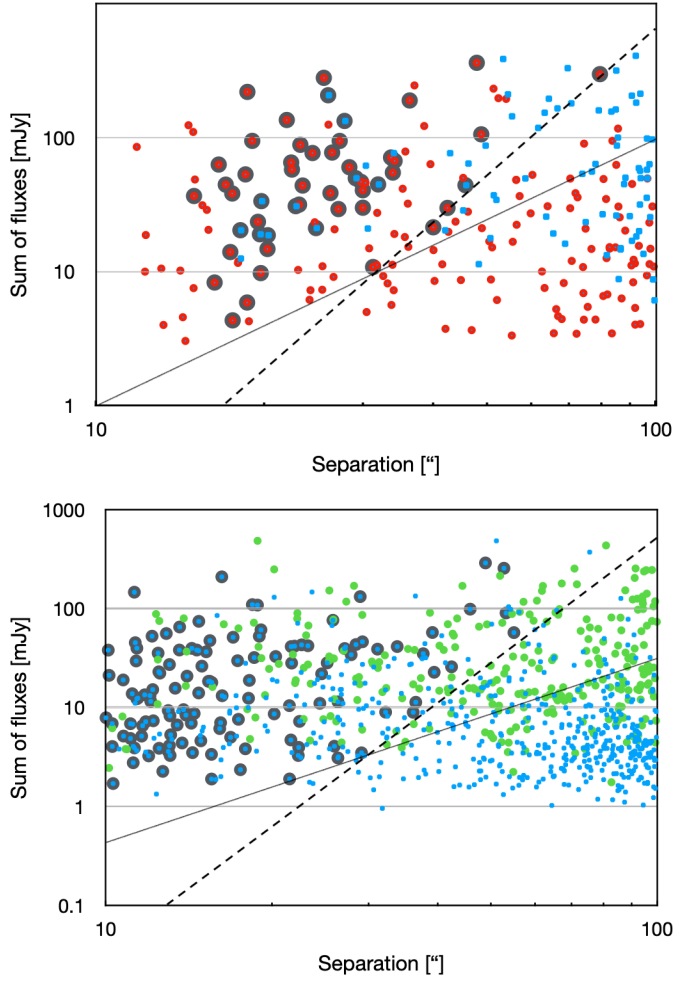


Fig. 13. Sum of flux densities from pairs of nearby sources (FS) vs source separation (x). Top panel: for 325 MHz sources; in red, pairs of sources with flux ratio (integrated/peak) below 4; in blue, the rest; larger dark grey circles: pairs of confirmed double sources (see text). Dashed line: $(x/16)^{3.5}$. Thin solid line: $(x/10)^2$. Bottom panel: for 610 MHz sources; in green, pairs of sources with flux ratio below 4; in blue, the rest; larger dark grey circles: pairs of double sources (see text). Dashed line: $(x/20)^{3.5}$. Thin solid line: $(x/16)^2$.

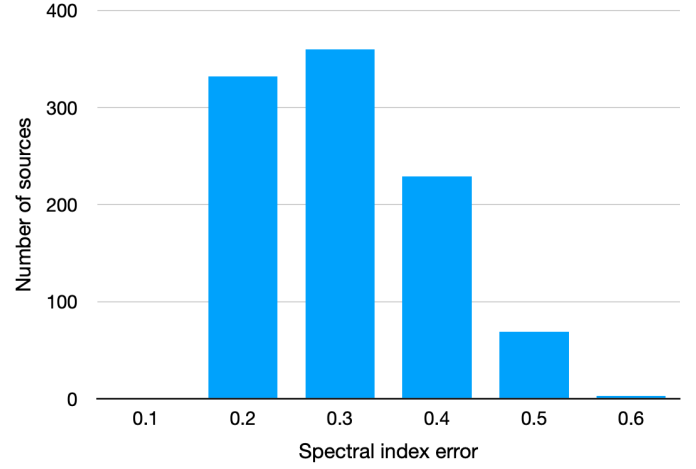


Fig. 15. Distribution of spectral index errors corresponding to the sources detected at both frequency bands (see Table 5).

at 325 MHz, for 52 sources only detected at 610 MHz, and for 86 sources detected at both bands, ordered by right ascension. The angular distance d between the GMRT source and the potential counterpart and the spectral index -if applicable- is also listed. By looking in the literature, we investigated the nature of the potential counterpart, and proposed whenever possible the more plausible object that could be associated with the GMRT sources reported here, along with its reference or, in the worst case, the reference of flux measured at other wavelength(s). In the cases with pre-existing 325-MHz observations, we quote no counterpart, since the present observations superseded them in sensitivity or also in angular resolution. Besides information from the surveys already mentioned in Sect. 2, valuable material was found in Vollmer et al. (2010), that compiles flux values of sources at the radio range including those of the Cygnus region relevant here, exception made of fluxes at the 610 MHz band, for which no previous data were found. In that sense, the present Catalog completes many radio spectra, providing for the first time 610-MHz flux values of ~ 2800 sources.

About the sources with possible counterparts that were detected at both frequencies, 16% have flat or positive spectral index (nominally, $\alpha > -0.2$). Their counterparts are mostly either stars, young stellar objects, or radio sources detected at larger frequencies.

At the 325 MHz band, the number of sources here found with possible counterparts was 8% of all the 325 MHz catalogued sources. At 610 MHz, the number of sources with possible counterparts resulted in 5% of all the 610 MHz catalogued sources. These low percentages can be explained considering that at the observed bands -decimetre wavelengths-, we are sampling mostly non-thermal sources, at which high energy (HE) processes are presumably taking place. These could be potential counterparts to the HE sources; but the angular resolutions and sensitivities for instruments working at HE ranges are larger, and poorer, respectively, precluding successful cross-identifications between radio and high-energy sources.

Preliminary results of a study focused on the unresolved unidentified sources with negative spectral index (~ 340 sources of the present catalog), like that performed by Chakraborty et al. (2020), pointed to differential source counts in the trend of distributions of extragalactic sources, as resulting from other surveys/catalogs. However, we recall that the observed fields are in the surroundings of the Galactic plane, dense in galactic sources, both of thermal and non-thermal nature. A detailed investigation to disentangle in which proportion and, more interesting, from which kind of objects, galactic and extragalactic sources are contributing etc is beyond the scope of this paper.

9. Related studies and prospects

The GMRT observations that gave rise to the Catalog of the present paper allowed at the same time to carry out research on individual population of astronomical objects. Specifically, different kinds of those that can produce non-thermal emission were or are being studied in separated investigations: AGNs and two-lobed sources, counterparts to high-energy sources, massive early-type stars (Benaglia et al. 2020), protoplanetary disk-like sources (Isequilla et al. 2019) and Young Stellar Objects (Isequilla et al. 2020). Finally, the survey images will be presented elsewhere. Future work includes the scrutiny of sources between 3 and 7σ . The corresponding source extraction, after a thorough validation process, of such a large area with the few-arcsec angular resolution provided by the GMRT data at decimetre frequencies, will certainly reveal a plethora of interesting objects and powerful statistical results of the non-thermal sky.

Acknowledgements. The authors are grateful to the referee, whose comments and suggestions resulted in improving the analysis and presentation of the article. The GMRT is operated by the National Centre for Radio Astrophysics of the Tata Institute of Fundamental Research. We thank the staff of the GMRT that made these observations possible. PB acknowledges support from ANPCyT PICT 0773–2017, and the contacts at NCRA, Pune for a very pleasant stay. ICCH acknowledges the support of the Department of Atomic Energy, Government of India, under the project 12-R&D-TFR-5.02-0700. This research has made use of the SIMBAD database, operated at CDS, Strasbourg, France, and of NASA's Astrophysics Data System bibliographic services.

References

Abeysekara, A. U., Archer, A., Aune, T., et al. 2018, *ApJ*, 861, 134
 Albacete Colombo, J. F., Flaccomio, E., Micela, G., Sciortino, S., & Damiani, F. 2007, *A&A*, 464, 211
 Anderson, L. D., Armentrout, W. P., Johnstone, B. M., et al. 2015, *ApJS*, 221, 26
 Araudo, A. T., Romero, G. E., Bosch-Ramon, V., & Paredes, J. M. 2007, *A&A*, 476, 1289
 Becker, R. H., White, R. L., & Helfand, D. J. 1995, *ApJ*, 450, 559
 Benaglia, P., De Becker, M., Ishwara-Chandra, C. H., Intema, H., & Isequilla, N. 2020, *PASA*, 38, 1
 Benaglia, P., del Palacio, S., Ishwara-Chandra, C. H., et al. 2019, *A&A*, 625, A99
 Benaglia, P. & Romero, G. E. 2003, *A&A*, 399, 1121

Benaglia, P., Romero, G. E., Martí, J., Peri, C. S., & Araudo, A. T. 2010, *A&A*, 517, L10
 Bosch-Ramon, V., Romero, G. E., Araudo, A. T., & Paredes, J. M. 2010, *A&A*, 511, A8
 Brinkmann, W., Siebert, J., Feigelson, E. D., et al. 1997, *A&A*, 323, 739
 Bulgarelli, A., Fioretti, V., Parmiggiani, N., et al. 2019, *A&A*, 627, A13
 Chakraborty, A., Roy, N., Wang, Y., et al. 2020, *MNRAS*, 492, 2236
 Chandra, P., Ray, A., & Bhatnagar, S. 2004, *ApJ*, 612, 974
 Chen, A. M., Takata, J., Yi, S. X., Yu, Y. W., & Cheng, K. S. 2019, *A&A*, 627, A87
 Clegg, A. W., Cordes, J. M., Simonetti, J. M., & Kulkarni, S. R. 1992, *ApJ*, 386, 143
 Colley, D. 1980, *MNRAS*, 192, 377
 Comerón, F., Pasquali, A., Rodighiero, G., et al. 2002, *A&A*, 389, 874
 Condon, J. J., Cotton, W. D., Greisen, E. W., et al. 1998, *AJ*, 115, 1693
 Cutri, R. M., Skrutskie, M. F., van Dyk, S., et al. 2003, *VizieR Online Data Catalog*, II/246
 De Becker, M. & Raucq, F. 2013, *A&A*, 558, A28
 del Palacio, S., Bosch-Ramon, V., Müller, A. L., & Romero, G. E. 2018, *A&A*, 617, A13
 del Valle, M. V. & Pohl, M. 2018, *ApJ*, 864, 19
 Douglas, J. N., Bash, F. N., Bozayan, F. A., Torrence, G. W., & Wolfe, C. 1996, *AJ*, 111, 1945
 Elyajouri, M., Monreal-Ibero, A., Remy, Q., & Lallement, R. 2016, *ApJS*, 225, 19
 Garwood, R. W., Perley, R. A., Dickey, J. M., & Murray, M. A. 1988, *AJ*, 96, 1655
 Greaves, J. 2004, *MNRAS*, 355, 585
 Hartman, R. C., Bertsch, D. L., Bloom, S. D., et al. 1999, *ApJS*, 123, 79
 Haslam, C. G. T., Salter, C. J., Stoffel, H., & Wilson, W. E. 1982, *A&AS*, 47, 1
 Hermsen, W., Swanenburg, B. N., Bignami, G. F., et al. 1977, *Nature*, 269, 494
 Higgs, L. A., Wendker, H. J., & Landecker, T. L. 1994, *A&A*, 291, 295
 Hög, E., Fabricius, C., Makarov, V. V., et al. 2000, *A&A*, 355, L27
 Huynh, M. T., Jackson, C. A., Norris, R. P., & Prandoni, I. 2005, *AJ*, 130, 1373
 Immer, K., Brunthaler, A., Reid, M. J., et al. 2011, *ApJS*, 194, 25
 Intema, H. T. 2014, SPAM: Source Peeling and Atmospheric Modeling, *Astrophysics Source Code Library*
 Isequilla, N. L., Benaglia, P., Ishwara-Chandra, C. H., & Intema, H. 2020, *Boletín de la Asociación Argentina de Astronomía*, 61B, 1
 Isequilla, N. L., Fernández-López, M., Benaglia, P., Ishwara-Chandra, C. H., & del Palacio, S. 2019, *A&A*, 627, A58
 Ishwara-Chandra, C. H., Benaglia, P., De Becker, M., & Tej, A. 2019, *Bulletin de la Société Royale des Sciences de Liège*, 88, 166
 Johnston, K. G., Shepherd, D. S., Robitaille, T. P., & Wood, K. 2013, *A&A*, 551, A43
 Knödseder, J. 2000, *A&A*, 360, 539
 Kohoutek, L. 2001, *A&A*, 378, 843
 Kryukova, E., Megeath, S. T., Hora, J. L., et al. 2014, *AJ*, 148, 11
 Lu, X., Zhang, Q., Liu, H. B., Wang, J., & Gu, Q. 2014, *ApJ*, 790, 84
 Magliocchetti, M., Maddox, S. J., Lahav, O., & Wall, J. V. 1998, *MNRAS*, 300, 257
 Mahy, L., Rauw, G., De Becker, M., Eenens, P., & Flores, C. A. 2013, *A&A*, 550, A27
 Martí, J., Pérez-Ramírez, D., Luque-Escamilla, P., et al. 2006, *A&A*, 451, 1037
 Massaro, F., D'Abrusco, R., Giroletti, M., et al. 2013, *ApJS*, 207, 4
 Melikian, N. D., Tamazian, V. S., Karapetian, A. A., Samsonian, A. L., & Kostandian, G. R. 2011, *Astrophysics*, 54, 203
 Mitronova, S. N., Karachentsev, I. D., Karachentseva, V. E., Jarrett, T. H., & Kudrya, Y. N. 2004, *Bulletin of the Special Astrophysics Observatory*, 57, 5
 Montes, V. A., Hofner, P., Anderson, C., & Rosero, V. 2015, *ApJS*, 219, 41
 Neria, C., Gómez, Y., & Rodríguez, L. F. 2010, *Rev. Mexicana Astron. Astrofis.*, 46, 253
 Panessa, F., Tarchi, A., Castangia, P., et al. 2015, *MNRAS*, 447, 1289
 Paredes, J. M., Martí, J., Ishwara-Chandra, C. H., et al. 2008, *A&A*, 482, 247
 Parthasarathy, M., Jain, S. K., & Bhatt, H. C. 1992, *A&A*, 266, 202
 Paunzen, E. 2015, *A&A*, 580, A23
 Price-Whelan, A. M., Hogg, D. W., Rix, H.-W., et al. 2018, *AJ*, 156, 18
 Purcell, C. R., Hoare, M. G., Cotton, W. D., et al. 2013, *ApJS*, 205, 1
 Ramachandran, V., Das, S. R., Tej, A., et al. 2017, *MNRAS*, 465, 4753
 Rauw, G. 2011, *A&A*, 536, A31
 Reddish, V. C., Lawrence, L. C., & Pratt, N. M. 1966, *Publications of the Royal Observatory of Edinburgh*, 5, 111
 Reipurth, B. & Schneider, N. 2008, *Star Formation and Young Clusters in Cygnus*, ed. Reipurth, B. (ASP), 36
 Rengelink, R. B., Tang, Y., de Bruyn, A. G., et al. 1997, *A&AS*, 124, 259
 Rodríguez-Kamenetzky, A., Carrasco-González, C., González-Martín, O., et al. 2019, *MNRAS*, 482, 4687
 Romero, G. 2008, *Gamma rays from star forming regions*, ed. Aharonian, F.A. (AIP), 97

- Romero, G. E., Torres, D. F., Kaufman Bernadó, M. M., & Mirabel, I. F. 2003, *A&A*, 410, L1
- Sánchez-Monge, Á., Palau, A., Estalella, R., Beltrán, M. T., & Girart, J. M. 2008, *A&A*, 485, 497
- Scaife, A. M. M. & Heald, G. H. 2012, *MNRAS*, 423, L30
- Setia Gunawan, D. Y. A., de Bruyn, A. G., van der Hucht, K. A., & Williams, P. M. 2003, *ApJS*, 149, 123
- Solin, O., Ukkonen, E., & Haikala, L. 2012, *A&A*, 542, A3
- Swarup, G., Ananthakrishnan, S., Kapahi, V. K., et al. 1991, *Current Science*, 60, 95
- Taylor, A. R., Goss, W. M., Coleman, P. H., van Leeuwen, J., & Wallace, B. J. 1996, *ApJS*, 107, 239
- The Fermi-LAT collaboration. 2019, arXiv e-prints, arXiv:1902.10045
- Urquhart, J. S., Hoare, M. G., Purcell, C. R., et al. 2009, *A&A*, 501, 539
- Uyaniker, B., Fürst, E., Reich, W., Aschenbach, B., & Wielebinski, R. 2001, *A&A*, 371, 675
- Verbeek, K., Groot, P. J., Scaringi, S., et al. 2012, *MNRAS*, 426, 1235
- Véron-Cetty, M. P. & Véron, P. 2010, *A&A*, 518, A10
- Vollmer, B., Gassmann, B., Derrière, S., et al. 2010, *A&A*, 511, A53
- Wendker, H. J., Higgs, L. A., & Landecker, T. L. 1991, *A&A*, 241, 551
- Williams, P. K. G., Bower, G. C., Croft, S., et al. 2013, *ApJ*, 762, 85
- Wright, N. J., Drake, J. J., Drew, J. E., et al. 2012, *ApJ*, 746, L21
- Zhang, Q., Claus, B., Watson, L., & Moran, J. 2017, *ApJ*, 837, 53
- Zoonematkermani, S., Helfand, D. J., Becker, R. H., White, R. L., & Perley, R. A. 1990, *ApJS*, 74, 181

Table 6. Counterparts of detected sources at 325 MHz and 610 MHz.

325-ID BIC325-	610-ID BIC610-	Spectral index	RA _{J2000} (h,m,s)	Dec _{J2000} (deg,′,″)	<i>d</i> (″)	SIMBAD nearest source	Reference	Information on possible nature
—	0045	—	20:12:57.27	41:51:49.34	4.6	2MFGC 15386	Mitronova et al. (2004)	disk-like galaxy
—	0093	—	20:13:47.77	41:10:02.13	7.6	CXO J201348.3+411007.1	Montes et al. (2015)	X-ray source
0006	0124	-1.0 ± 0.1	20:14:18.68	41:18:11.26	5.4	CXO J201419.1+411813.4	Montes et al. (2015)	star-forming region
—	0217	—	20:15:21.60	40:34:43.93	6.8	PN KJpN 2	Kohoutek (2001)	planetary nebula
0107	0429	-1.0 ± 0.3	20:17:54.12	41:24:14.49	5.3	J201754.59+412413.98	Kryukova et al. (2014)	IR source
0119	0462	-1.6 ± 0.2	20:18:07.79	41:10:41.13	5.2	FGL J2018.1+4111	Abeysekara et al. (2018)	γ-ray source
0134	0531	-2.4 ± 0.1	20:18:38.18	40:41:00.42	3.7	MSX6C G078.0875+02.6408	Panessa et al. (2015)	Seyfert galaxy
—	0543	—	20:18:42.69	44:17:34.13	2.2	NVSS J201842+441736	Vollmer et al. (2010)	
—	0551	—	20:18:46.65	42:20:04.91	8.2	NVSS J201847+422010	Condon et al. (1998)	
—	0582	—	20:19:02.55	40:18:26.02	4.1	WSRTGP 2017+4009	Vollmer et al. (2010)	
0151	0624	-0.2 ± 0.3	20:19:19.30	40:54:51.52	7.8	MTK2011-F114	Melikian et al. (2011)	
0162/0163/0164	0665/0666/0672	-1.0 ± 0.2	20:19:36.50	40:58:50.00	~10	NGR2010-VLAN 2,3	Neria et al. (2010)	emission-line star
0165	0676	+0.9 ± 0.1	20:19:38.89	40:56:36.21	1.3	IRAS 20178+4046-VLAN 4	Neria et al. (2010)	UC HII region
0170	0690	-1.0 ± 0.1	20:19:49.33	42:00:12.26	5.0	J201949.77+420011.20	Kryukova et al. (2014)	UC HII region
—	0731	—	20:20:09.10	43:40:22.78	2.0	RX J2020.0+4357	Brinkmann et al. (1997)	YSO
0182	0757	+0.1 ± 0.2	20:20:18.62	40:58:03.26	5.3	J202019.08+405802.18	Kryukova et al. (2014)	X-ray source
—	0787	—	20:20:27.95	43:51:13.88	2.4	WR 140	De Becker & Rauq (2013)	YSO
0196	0808	+0.3 ± 0.1	20:20:35.65	40:57:54.84	6.2	J202036.15+405753.58	Kryukova et al. (2014)	WR system
"	"	"	20:20:36.18	40:57:53.08	6.6	NVSS J202036+405754	Vollmer et al. (2010)	YSO
—	0825	—	20:20:42.59	42:16:46.54	8.0	MITG J2020+4216	Vollmer et al. (2010)	
0200	0842	-0.0 ± 0.3	20:20:51.07	41:22:05.96	5.6	J202051.55+412204.76	Kryukova et al. (2014)	YSO
—	0861	—	20:20:57.67	44:41:29.82	0.9	NVSS J202057+444130	Vollmer et al. (2010)	
—	0894	—	20:21:18.24	41:19:59.65	5.0	J202118.68+411958.86	Kryukova et al. (2014)	YSO
—	0967	—	20:21:49.02	44:00:37.37	2.7	2MASX J20214907+4400399	Véron-Cetty & Véron (2010)	Seyfert galaxy
—	1049	—	20:22:17.22	42:24:49.47	10.4	18P 22	Vollmer et al. (2010)	
0263	1051	-0.1 ± 0.2	20:22:17.85	43:53:01.09	8.3	2MASS J20221736+4353074	Price-Whelan et al. (2018)	red giant star
—	1112	—	20:22:44.55	41:45:17.41	5.9	J202245.07+414517.98	Kryukova et al. (2014)	YSO
—	1117	—	20:22:46.33	41:07:00.44	5.8	J202245.07+414517.98	Kryukova et al. (2014)	YSO
—	1126	—	20:22:52.35	44:48:20.56	3.3	BD+44 3444	Elyajouri et al. (2016)	B8 star
—	1205	—	20:23:19.06	43:12:44.08	8.2	IRAS 20216+4303	Vollmer et al. (2010)	
0343	1248	+0.1 ± 0.1	20:23:35.68	41:25:26.43	3.3	J202335.81+412523.53	Kryukova et al. (2014)	YSO
0347	1253	-0.8 ± 0.1	20:23:39.05	44:01:04.49	10.6	18P 25	Vollmer et al. (2010)	
0393	1329	-1.2 ± 0.2	20:24:11.53	41:43:24.47	9.1	TYC 3160-519-1	Høg et al. (2000)	star
0390/0395	1334	-0.5 ± 0.1	20:24:15.43	43:22:32.22	5	NVSS J202415+432235	Vollmer et al. (2010)	
0434	1404	-0.6 ± 0.3	20:24:46.19	42:23:13.16	9.3	BD+41 3737	Paunzen (2015)	star
—	1420	—	20:24:52.00	40:40:25.21	5.6	G078.779+01.693	Anderson et al. (2015)	HII region
0460	1447	-0.7 ± 0.1	20:25:00.59	41:48:25.43	6.1	NVSS J202501+414829	Condon et al. (1998)	
0490	1493	+0.6 ± 0.1	20:25:19.02	43:35:19.40	4.7	J2025+4335	Immer et al. (2011)	
0496	1503	-0.8 ± 0.1	20:25:22.74	44:19:33.44	1.4	NVSS J202522+441934	Condon et al. (1998)	
0503	1511	-0.8 ± 0.2	20:25:24.78	41:03:19.48	3.6	G079.151+01.830	Solin et al. (2012)	star-forming region
0526	1557/1563	-1.1 ± 0.1	20:25:40.53	42:32:17.14	6.4	NVSS J202540+423222	Condon et al. (1998)	
—	1569	—	20:25:42.91	41:56:15.55	5.6	NVSS J202543+415618	Vollmer et al. (2010)	
—	1572	—	20:25:44.10	41:56:02.14	6.0	J202544.53+415605.70	Kryukova et al. (2014)	YSO

Table 6. continued.

325-ID BIC325-	610-ID BIC610-	Spectral index	RA _{J2000} (h,m,s)	Dec _{J2000} (deg,′,″)	<i>d</i> (″)	SIMBAD nearest source	Reference	Information on possible nature
0600	1680	-1.0 ± 0.1	20:26:25.48	42:32:09.42	5.2	NVSS J202625+423214	Condon et al. (1998)	
0604	1685	-0.8 ± 0.1	20:26:26.26	44:39:27.16	3.9	NVSS J202625+443927	Vollmer et al. (2010)	
0626	1728	-0.9 ± 0.1	20:26:42.98	40:51:28.03	10.5	NVSS J202642+405138	Vollmer et al. (2010)	
—	1821	—	20:27:18.99	40:25:00.97	1.0	WSRTGP 2025+4015	Vollmer et al. (2010)	star
0684	1822	-1.1 ± 0.1	20:27:19.57	43:13:58.44	14.3	TYC 3164-341-1	Høg et al. (2000)	IR source
0722	1908	-0.8 ± 0.1	20:27:52.92	41:35:05.03	5.2	J202753.37+413506.03	Kryukova et al. (2014)	YSO
0735	1944	-0.4 ± 0.1	20:28:04.06	41:13:54.24	5.1	J202804.51+411354.56	Kryukova et al. (2014)	white dwarf
0744	1957	-0.8 ± 0.1	20:28:07.20	41:13:50.64	7.9	UVEX J202807.55+411357.7	Verbeek et al. (2012)	
—	1967	—	28:28:10.38	45:12:51.73	0.2	NVSS J202810+451251	Condon et al. (1998)	
—	1980	—	20:28:13.29	40:16:52.83	3.6	WSRTGP 2026+4006	Vollmer et al. (2010)	
0769	2013	-1.1 ± 0.1	20:28:24.34	40:37:50.03	3.9	19P 6	Wendker et al. (1991)	YSO
—	2027	—	20:28:31.01	40:59:59.05	3.9	J202831.35+405959.24	Kryukova et al. (2014)	star
0788	2068	-1.1 ± 0.1	20:28:49.60	41:18:37.36	0.6	TYC 3160-1079-1	Høg et al. (2000)	
0789	2070	-1.3 ± 0.1	20:28:50.79	41:34:37.13	5.5	NVSS J202851+413438	Vollmer et al. (2010)	
0804	2108	-1.1 ± 0.1	20:29:00.90	42:12:59.28	5.5	NVSS J202901+421259	Condon et al. (1998)	
0806	2115	-0.9 ± 0.1	20:29:04.20	41:00:05.78	4.1	19P 7	Wendker et al. (1991)	star
0807	2118	-1.0 ± 0.1	20:29:04.70	42:35:27.90	4.4	TYC 3160-1447-1	Høg et al. (2000)	star-forming region
—	2159	—	20:29:23.53	40:11:09.57	4	AFGL 2591	Johnston et al. (2013)	
—	2170	—	20:29:28.60	40:57:24.41	7.0	19P 9	Wendker et al. (1991)	
—	2174	—	20:29:30.94	41:34:20.72	5.2	J202931.39+413421.96	Kryukova et al. (2014)	YSO
—	2189	—	20:29:36.50	41:51:40.89	4.6	WSRTGP 2027+4141	Vollmer et al. (2010)	
0846	2215	-1.7 ± 0.3	20:29:49.42	41:43:13.66	16.7	** GRV 344	Greaves (2004)	stellar system
—	2223	—	20:29:52.06	40:48:45.82	2.7	G079.4430+01.0047	Urquhart et al. (2009)	HII region
0854	—	—	20:29:59.18	41:16:44.20	7.0	IRAS 20286+4105	Ramachandran et al. (2017)	star-forming region
0867	2280	-0.9 ± 0.1	20:30:14.17	40:41:08.67	10.4	IRAS 20283+4031	Parthasarathy et al. (1992)	star
0872	2299	-1.2 ± 0.1	20:30:30.47	44:12:26.40	4.9	2MASS J20303018+4412301	Price-Whelan et al. (2018)	star
0873	2311	-0.7 ± 0.1	20:30:36.58	41:06:06.10	6.2	NVSS J203032+410634	Williams et al. (2013)	
—	2313	—	20:30:37.68	42:20:57.96	15.9	WSRTGP 2028+4211	Vollmer et al. (2010)	
0874	2319	-0.8 ± 0.1	20:30:39.72	41:23:31.73	0.4	NVSS J203039+412331	Vollmer et al. (2010)	YSO
—	2351	—	20:30:57.60	43:08:05.33	6.9	WSRTGP 2029+4257	Vollmer et al. (2010)	star
0882	2370	-2.1 ± 0.3	20:31:10.22	40:58:53.80	2.5	J203110.44+405853.94	Kryukova et al. (2014)	star
—	2376	—	20:31:14.29	42:22:42.95	4.1	TYC 3161-82-1	Høg et al. (2000)	
0889	2381	-1.0 ± 0.2	20:31:18.69	41:09:25.16	10.7	RLP 933	Reddish et al. (1966)	
—	2382	—	20:31:19.14	40:18:09.90	0.4	IRAS 20293+4007 VLA 3	Sánchez-Monge et al. (2008)	
0890	2384	-1.0 ± 0.1	20:31:19.90	40:40:56.04	1.6	GPSR 079.501+0.704	Zoonematkermani et al. (1990)	wind shell
—	2406	—	20:31:37.33	40:22:58.79	0.3	G79.29+0.46	Higgs et al. (1994)	wind shell
—	2409	—	20:31:39.72	40:16:08.36	0.2	G79.29+0.46	Higgs et al. (1994)	X-ray star
—	2420	—	20:31:51.59	41:31:18.60	2.8	BDB 2006-234	Paredes et al. (2008)	galaxy S lobe
0906	2432	-1.4 ± 0.1	20:32:00.50	41:36:58.45	1.0	J203201.7+413722	Paredes et al. (2008)	galaxy N lobe
0908	2435	-1.4 ± 0.1	20:32:01.91	41:37:47.43	1.0	J203201.7+413722	Paredes et al. (2008)	Be star+pulsar
0915	2448	-2.1 ± 0.4	20:32:12.92	41:27:24.01	2.3	MT91-213	Chen et al. (2019)	
—	2452	—	20:32:14.13	40:42:24.88	0.7	NVSS J203214+404226	Vollmer et al. (2010)	part of nebula
—	2463	—	20:32:21.17	40:17:18.63	0.5	DR 151	Colley (1980)	

Table 6. continued.

325-ID BIC325-	610-ID BIC610-	Spectral index	RA _{J2000} (h,m,s)	Dec _{J2000} (deg,′,″)	<i>d</i> (″)	SIMBAD nearest source	Reference	Information on possible nature
0921	2464	-0.5 ± 0.2	20:32:22.32	41:18:19.28	1.2	Cyg OB2 5	De Becker & Rauq (2013)	OB stellar system
0924	2469	+1.4 ± 0.1	20:32:25.65	40:57:28.09	1.5	WR 145a	Bulgarelli et al. (2019)	HMXB
0925	2470	-0.5 ± 0.1	20:32:26.77	41:04:33.28	1.3	HSC N	Martí et al. (2006)	part of cloud
0927	2472	-1.3 ± 0.2	20:32:29.25	41:35:07.36	1.7	2MASS J20322935+4135061	Cutri et al. (2003)	IR source
0928	2473	-0.1 ± 0.3	20:32:29.52	40:38:49.65	0.9	GPSR 079.602+0.506	Zoonmatkermani et al. (1990)	
0933	—	—	20:32:36.60	41:14:47.87	14.4	RLP 886	Reddish et al. (1966)	star
—	2494	—	20:32:40.83	41:14:29.31	1.4	Cyg OB2 12	De Becker & Rauq (2013)	star
0941	2501	+0.6 ± 0.1	20:32:45.44	40:39:37.50	1.3	EM* MWC 349	Zhang et al. (2017)	emission-line star
0946	2514	-0.9 ± 0.1	20:32:55.32	40:31:30.99	4.6	19P 22	Wendker et al. (1991)	
0953	2526	-1.1 ± 0.1	20:33:10.27	40:41:16.91	1.9	J203310.31+404118.72	Kryukova et al. (2014)	YSO
”	2528	”	20:33:11.01	40:41:32.23	4.8	19P 24	Vollmer et al. (2010)	
”	2530	”	20:33:11.74	40:41:49.35	2.1	J203311.80+404151.32	Kryukova et al. (2014)	YSO
—	2536	—	20:33:14.93	41:18:50.63	1.7	Cyg OB2 8A	De Becker & Rauq (2013)	OB stellar system
0956	2544/2545	-0.3 ± 0.1	20:33:18.92	40:58:37.39	14.4	G079.964+00.579	Anderson et al. (2015)	
0957	2545	-0.4 ± 0.1	20:33:19.00	40:59:05.06	13.6	G079.964+00.579	Anderson et al. (2015)	
”	—	—	20:33:19.00	40:59:05.06	15.5	BD+40 4230	Reddish et al. (1966)	star
0963	2552/2556/2558	-1.2 ± 0.1	20:33:23.42	41:27:17.60	6.6	19P 26	Vollmer et al. (2010)	
”	—	”	20:33:23.42	41:27:17.60	22.3	IDX 114	Rauw (2011)	X-ray star
0965	2559	-0.8 ± 0.3	20:33:24.95	40:57:28.81	8.3	RLP 1034	Reddish et al. (1966)	star
0966	2560	-0.5 ± 0.3	20:33:26.58	40:42:33.04	1.8	J203326.44+404233.74	Kryukova et al. (2014)	YSO
—	2565	—	20:33:30.74	41:35:28.42	8.5	RLP 283	Reddish et al. (1966)	star
0968	2566	-0.3 ± 0.1	20:33:31.97	40:41:03.03	8.2	19P 28	Wendker et al. (1991)	
0976	2585	-1.4 ± 0.1	20:33:47.12	40:40:54.64	10.6	J203348.01+404051.61	Kryukova et al. (2014)	YSO
0977	2589	-0.9 ± 0.1	20:33:52.22	41:15:45.11	7.7	AFM2007-990	Albacete Colombo et al. (2007)	X-ray star
—	2603	—	20:34:06.69	41:16:00.86	1.0	J203406.77+411600.46	Kryukova et al. (2014)	YSO
0985	2607	-0.3 ± 0.2	20:34:10.56	41:06:58.71	0.7	IPHASX J203410.5+410659	Wright et al. (2012)	frEGG
0988	2610	-2.5 ± 0.2	20:34:13.85	41:08:16.31	5.0	WDDGGHK7	Isequilla et al. (2019)	frEGG
1000	2635	-1.6 ± 0.2	20:34:36.48	40:51:59.24	5.3	WDDGGHK4	Isequilla et al. (2019)	frEGG
1003	2638	-1.3 ± 0.1	20:34:43.28	40:53:15.48	2.1	WDDGGHK3	Isequilla et al. (2019)	frEGG
—	2652	—	20:34:53.33	40:53:20.89	2.2	WDDGGHK2	Isequilla et al. (2019)	frEGG
1006	2641	-0.8 ± 0.3	20:34:45.15	41:45:03.2	3.2	GPSR 079.918+0.283	Zoonmatkermani et al. (1990)	
—	2625	—	20:34:29.54	41:31:45.2	0.7	TYC 3161-1048-1	Høg et al. (2000)	star
1012	2654	-0.6 ± 0.1	20:34:55.80	40:40:46.56	1.6	GPSR 079.904+0.154	Zoonmatkermani et al. (1990)	
—	2657	—	20:34:57.30	40:04:14.94	6.5	TYC 3157-1182-1	Høg et al. (2000)	star
1014	2659	+0.4 ± 0.1	20:35:00.28	41:34:52.90	2.34	IRAS 20332+4124	Lu et al. (2014)	star-forming region
1018	2663	-0.0 ± 0.2	20:35:02.77	41:34:51.22	10.8	IRAS 20332+4124	Lu et al. (2014)	star-forming region
1019	2664	-0.1 ± 0.2	20:35:03.56	41:18:24.12	0.4	2MASS J20350353+4118240	Cutri et al. (2003)	IR source
—	2666	—	20:35:07.84	39:59:48.46	2.8	GPSR 079.380-0.284	Zoonmatkermani et al. (1990)	
1020	2670	+0.9 ± 0.1	20:35:16.63	40:49:44.66	1.0	GPSR 080.063+0.191	Zoonmatkermani et al. (1990)	
1024	2680	-1.2 ± 0.1	20:35:32.37	41:44:56.33	0.8	NVSS J203532+414456	Condon et al. (1998)	
1025	—	—	20:35:33.17	41:06:45.07	2.8	GPSR 080.322+0.319	Vollmer et al. (2010)	
1027	—	—	20:35:42.72	40:52:51.58	1.7	GPSR 080.154+0.156	Zoonmatkermani et al. (1990)	
1030	2689	+0.2 ± 0.2	20:35:47.07	41:22:45.01	0.4	WR 146	De Becker & Rauq (2013)	WR system

Table 6. continued.

325-ID BIC325-	610-ID BIC610-	Spectral index	RA _{J2000} (h,m,s)	Dec _{J2000} (deg,′,″)	<i>d</i> (″)	SIMBAD nearest source	Reference	Information on possible nature
—	2693	—	20:35:55.32	42:18:03.67	3.5	2034+42A	Clegg et al. (1992)	
—	2697	—	20:35:58.48	42:17:23.86	3.1	2034+42B	Clegg et al. (1992)	
1032	2698	-0.6 ± 0.2	20:35:59.52	40:54:00.86	12.5	J203558.60+405353.85	Kryukova et al. (2014)	YSO
"	"	"	20:36:01.31	40:53:56.79	4.4	J203600.94+405358.24	Kryukova et al. (2014)	YSO
"	2700	"	20:36:01.31	40:53:56.79	8.1	J203601.85+405351.48	Kryukova et al. (2014)	YSO
1034	2707	+0.2 ± 0.2	20:36:12.84	40:45:43.14	2.1	GPSR 080.115+0.009	Zoonematkermani et al. (1990)	
1038	2721	-0.6 ± 0.1	20:36:29.72	41:20:21.90	0.5	CPR2002-B3	Comerón et al. (2002)	star
1039	2722	-1.2 ± 0.1	20:36:34.45	41:32:22.66	10.9	G080.522+00.714	Zoonematkermani et al. (1990)	
—	2730	—	20:36:43.72	40:21:09.99	2.6	WR 147	De Becker & Rauq (2013)	WR system
—	2770	—	20:37:37.72	40:53:52.54	1.8	080.386-0.122	Garwood et al. (1988)	
—	2785	—	20:37:58.29	40:00:52.85	2.9	18P6	Vollmer et al. (2010)	
—	2793	—	20:38:22.23	40:16:16.95	2.0	GPSR 079.972-0.614	Zoonematkermani et al. (1990)	